Dynamic Tuning and Symmetry Lowering of Fano Resonance in Plasmonic Nanostructure

Yonghao Cui, Jianhong Zhou, Venkata A. Tamma, and Wounjhang Park*

Department of Electrical, Computer and Energy Engineering, University of Colorado at Boulder, Boulder, Colorado 80309, United States

ABSTRACT We present dynamic tuning and symmetry lowering of Fano resonances in gold heptamers accomplished by applying uniaxial mechanical stress. The flexible heptamer structure was obtained by embedding the seven-gold-nanocylinder complex in a polydimethylsiloxane membrane. Under uniaxial stress, the Fano resonance exhibited opposite spectral shifts for the two orthogonal polarizations parallel and perpendicular to the mechanical stress. Furthermore, a new resonance was observed for polarization parallel to the mechanical stress but not for the perpendicular polarization. The experimental results showed good agreement with the numerical simulations. A detailed group theoretical analysis showed that the symmetry lowering caused by the mechanical stress not only splits the originally degenerate mode but also modifies the originally optically inactive mode into an optically active mode, which then interacts strongly with a closely spaced mode and exhibits anticrossing behavior. The symmetry tuning enabled by applying mechanical stress is a simple and efficient way to engineer the nature of coupled plasmon resonances in complex nanostructures. The mechanically tunable plasmonic nanostructures also provide an excellent platform for dynamically tunable nanophotonic devices such as tunable filters and sensors.

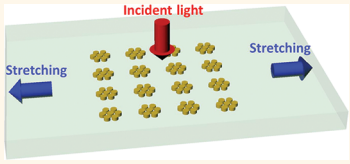

KEYWORDS: surface plasmon · Fano resonance · mechanical tuning · plasmonic nanostructure · localized surface plasmon resonance · anticrossing

Complex metallic nanostructures supporting a collective surface plasmon resonance are currently a topic of strong research interest. In this system, the surface plasmon resonances of constituent elements couple together to form collective modes delocalized over the entire structure. The characteristics of the collective plasmon modes are strong functions of the details of the nanostructure, opening new opportunities to investigate the interaction between plasmonic nanostructures and also to engineer the nature of the resonance for various applications, for example, in sensing and nonlinear devices. Much of the current research has been directed to metal nanoparticle aggregates in which the nanoparticle size, spacing between the nanoparticles, and symmetry of the aggregate could lead to different coupled plasmon modes.[1−14] The high sensitivity to the structural parameters is of special interest because it makes the system an excellent candidate for mechanically tunable devices. Structural tuning by mechanical stress is a natural way to achieve wide tunability in artificial materials and structures, which derive their properties from structural design. Mechanical tuning has been applied to photonic crystals, which exhibit many novel properties stemming from their periodicity.[15,16] Recently, tunable negative index imaging by a flexible photonic crystal has been reported.[17] Similar strategies have also been applied to metamaterials in which plasmonic nanostructures were subject to mechanical stress to distort and tune their resonances and thereby achieve a tunable metamaterial response.[18,19] It therefore seems only natural to explore the mechanical tuning of plasmonic nanostructures whose resonance is highly sensitive to their structural parameters, and mechanically tunable resonances have been demonstrated for a dolmen-type resonator[18] and nanoparticle dimer.[20]

Fano resonances,[21] which arise from the interference of a sharp resonance with a broad background, have attracted a great deal of research interest recently due to their asymmetric line shape, sharp resonance, and sensitivity to a variety of parameters. Traditionally Fano resonances have been considered mostly in quantum systems.[22−24] However, Fano resonances have recently been realized in plasmonic nanostructures and metamaterials.[2,5−14,18,25−31] Due to its narrow line width and high sensitivity to structural and environmental parameters, a Fano resonance has great potential for photonic applications such as sensing.[32] It has been reported that in many nanoparticle aggregates the collective plasmon modes exhibit a Fano resonance.[2,5−8,18] A heptamer is one of the reported metal nanoclusters that support a Fano resonance,[5−14] and it is predicted to exhibit a very large Fano resonance spectral

* Address correspondence to won.park@colorado.edu.

Received for review November 29, 2011 and accepted February 16, 2012.

Published online February 16, 2012
10.1021/nn204647b

shift upon tuning of the surrounding media's refractive index.[8] A Fano resonance in a heptamer is also highly sensitive to the gaps between the metal nanoparticles[6] and the symmetry of the heptamer.[8] Therefore, the heptamer structure is a good candidate to demonstrate a tunable Fano resonance through refractive index tuning, structural tuning, and symmetry tuning. For tuning efficiency, refractive index tuning is limited by the small range of attainable refractive index changes, while mechanical tuning, which can tune the gaps between metal nanoparticles and the symmetry of the heptamer, can produce much wider tunability and is capable of tuning structural parameters and symmetry simultaneously. Symmetry breaking is of particular interest, as it could not only lead to resonance frequency shifts but also alter the fundamental characteristics of the modes, leading to dramatic changes in the optical properties. Recently the symmetry-breaking effects have been studied for gold nanoparticle trimers.[33,34]

In this paper, we report a dynamically tunable Fano resonance in a gold heptamer structure embedded in a flexible polymer membrane and present how the symmetry lowering induced by mechanical stress affects the tunability. The gold heptamer structure was composed of seven gold nanocylinders embedded in a flexible polydimethylsiloxane (PDMS) membrane. Thanks to the high elasticity of the PDMS membrane, the gaps between the gold nanocylinders could be accurately tuned by mechanically stretching the PDMS membrane, leading to tuning of the Fano resonance. The uniaxial stress also lowers the symmetry of the heptamer structures, causing the splitting of the originally degenerate modes and also turning an originally optically inactive mode into an optically active mode. The resultant split modes and the newly created optically active modes strongly interact with one another and lead to distinct polarization dependence. In the following, we present experimental results on mechanical tuning of a Fano resonance in a gold heptamer and provide a detailed theoretical study on the mode properties of the heptamer under mechanical stress that explains the observed behaviors.

RESULTS AND DISCUSSION

The gold heptamer was designed to have seven gold nanocylinders with a diameter of 150 nm and height of 80 nm. The gap between cylinders was designed to be 30 nm. For reliable optical characterizations, a massive array of gold heptamers was fabricated in an array covering an area of $400 \times 400\ \mu m^2$. The massive array is formed by an 8×8 array of heptamers with individual array size of $50 \times 50\ \mu m^2$. Figure 1a shows a schematic diagram of a free-standing PDMS membrane with an embedded array of heptamers. Scanning electron microscopy (SEM) confirmed that high-quality heptamers were

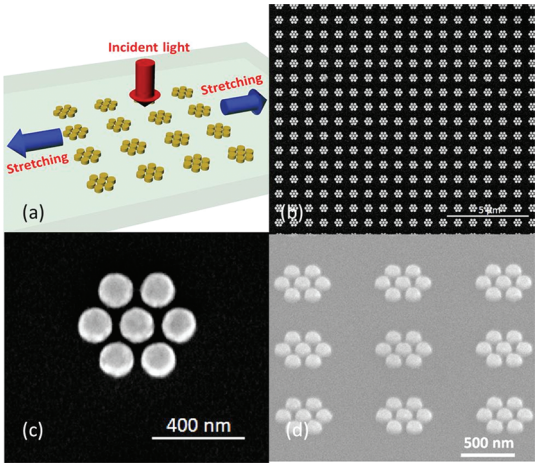

Figure 1. (a) Schematic diagram showing arrays of gold heptamers embedded in a PDMS membrane and being stretched, (b) SEM image showing arrays of gold heptamers at low magnification, (c) close-up SEM image of single gold heptamer from the top view, and (d) SEM image of 45° tilted 3×3 array of gold heptamers.

successfully fabricated with structural parameters close to the design values. Figure 1b–d shows the SEM images of the fabricated heptamer array. From the high-magnification SEM image shown in Figure 1c, the diameter of the gold cylinder was measured to be 147 nm. Figure 1c also shows that the heptamer structure was shrunk by 3.7% along the vertical direction and the gaps between the cylinders were 33 nm along the horizontal direction and 28 nm along the diagonal.

The heptamers were subsequently stretched along the horizontal direction in Figure 1c. The optical extinction spectra were taken for two orthogonal polarizations: parallel and perpendicular to the direction of mechanical stress. In the following discussion, we will refer to the horizontal and vertical directions in Figure 1c as *x* and *y* directions, respectively. The original heptamer structure is isotropic and thus should exhibit identical spectra for the two polarizations. However, due to the slight shrinkage of the actual fabricated heptamer along the *y* direction, there was a slight shift in spectra for the two orthogonal polarizations. As shown in Figure 2, the position of the Fano resonance, which presented itself as a dip in the extinction spectrum, was 829 nm for the *x* polarization, while the *y* polarization showed a dip at 838 nm. To confirm the small split was due to the imperfect fabrication, which resulted in a 3.7% shrinkage in the *y* direction, numerical simulations using the commercial software COMSOL were carried out. Figure 2 shows that the simulations accounting for the vertical shrinkage in the actual fabricated structure precisely reproduced the Fano resonance positions of experimentally measured spectra. The slight broadening in the experimental spectra was attributed to the slight size variations (less than 2%) among the heptamers in the array. Also, the nanostructured gold is expected to exhibit

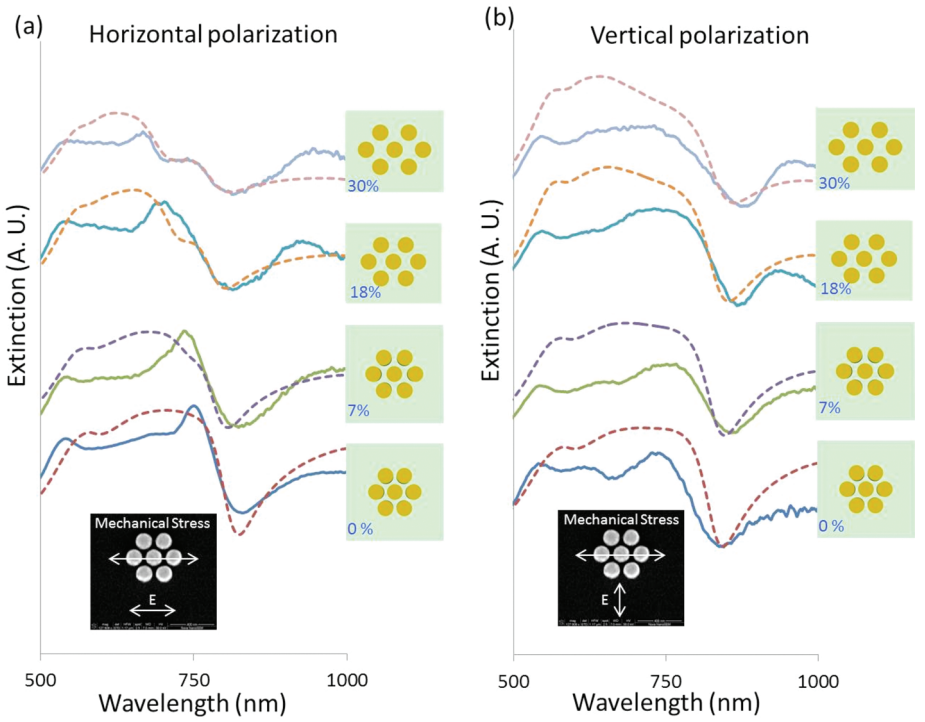

Figure 2. Experimentally measured and simulated extinction spectra for mechanical stress along the horizontal direction. Stretching direction and polarizations are shown in the insets. Solid lines show experiment results, and dashed lines show simulation results.

higher loss than the bulk, whose dielectric constants were used in the simulations.[35] This should account for some of the discrepancies between the experimental and simulation spectra. Overall, the agreement between the simulation and experiment was excellent.

The mechanical stress lowers the symmetry and increases the degeneracy, producing distinct behaviors for the two mutually orthogonal polarizations. Figure 2a shows experimentally measured and simulated extinction spectra at the induced mechanical strain values of 0%, 7%, 18%, and 30% with polarization parallel to the mechanical stress (*x* direction), as indicated in the inset of Figure 2a. The Fano resonance exhibited a moderate blue shift from 829 to 814 nm. Here, the mechanical strain is defined as the percent change in the center-to-center spacing between adjacent gold cylinders along the *x* direction. Experimentally, it is not possible to directly measure the strains. We therefore determine the strain values indirectly by first measuring the changes in the length of the heptamer array, which could be directly imaged by optical microscopy. In our experiments, the nominal values of strains measured this way were 11%, 28%, and 44%. However, the macroscopic geometrical deformation of the PDMS may not translate perfectly to the microscopic geometry of the heptamer structure. To determine the actual strain in the heptamers, we conducted mechanical simulations using COMSOL in which we modeled a single heptamer in a 900 nm × 900 nm size computational cell and applied the nominal strain values measured by the changes in array size. In the simulations, Young's modulus and Poisson's ratio were set to be 79 GPa and 0.44 for gold[36,37] and 360−870 kPa and 0.5 for PDMS.[38] Further details on the mechanical simulations may be found in the Supporting Information. For the nominal strain values of 11%, 28%, and 44% measured by the optical microscope, the simulations resulted in actual strains of 7%, 18%, and 30%, respectively, and these values were then used for optical simulations. Figure 2b shows the experiment and simulation spectra for the polarization perpendicular to the mechanical stress. In this case, the Fano resonance redshifted significantly from 838 to 874 nm. In addition to the spectral shifts in the opposite directions, the extinction spectra for the *x* polarization showed an additional feature at a shorter wavelength when the heptamer is under mechanical stress. This feature is noticeable at all strain values in simulations and also visible in experimental spectra for strain values of 18% and 30%. In contrast, this feature is clearly absent in all simulated and experimental spectra for *y* polarizations. The samples have been subject to multiple cycles of stress and release, and the optical spectra remained unchanged. The data are available in the Supporting Information.

To gain insight into the observed behavior, we conducted extensive theoretical studies by employing two complementary approaches. First, the eigenmodes of the heptamer structure were obtained in the static limit by solving the boundary integral eigenvalue equations for the charge distribution.[39,40]

This study allowed us to analyze the eigenmodes with the group representation theory and thus correlate the symmetry of the system with that of the eigenmodes. However, since this approach is valid only in the static limit, it cannot properly describe the retardation effects that must be taken into account in a system with large size features such as the heptamers investigated in this paper. For this purpose, we also conducted numerical simulations using generalized multiparticle Mie theory.[41] Since the multiparticle Mie theory can handle only spherical particles, the following theoretical studies deal with gold heptamers made of seven spheres, which should share all salient features of the gold cylinder heptamers in Figure 2. In all simulations, the experimentally determined dielectric function of gold was used.[35]

To briefly describe the boundary integral approach, for a system composed of an arbitrary array of N nanoparticles, the surface charge distribution $\sigma^j(\vec{r})$ of its jth surface plasmon mode satisfies the boundary-integral eigenvalue equation:[39,40]

$$\sigma^j(\vec{r}) = \frac{\lambda^j}{2\pi} \oint \sigma^j(\vec{r}_q) \frac{\vec{r} - \vec{r}_q}{|\vec{r} - \vec{r}_q|^3} \cdot \hat{n} dS_q \qquad (1)$$

where the integral is over the whole surfaces of the N nanoparticles and $\hat{n}$ is the unit vector normal to the surfaces of the N particles at point $\vec{r}$. The eigenvalue λ^j determines the system resonance frequency ω_j through the electric permittivity ε of the array by the relationship

$$\mathrm{Re}\,\varepsilon(\omega_j) = \varepsilon_b \left(\frac{1 + \lambda^j}{1 - \lambda^j} \right) \qquad (2)$$

where ε_b is the electric permittivity of the medium surrounding the nanoparticles. The eigenfunction $\sigma^j(\vec{r})$ describes the self-sustained surface charge distribution of the jth mode of the system. By solving eigenvalue eq 1 numerically,[39] we can analyze the symmetry of the modes.

Mirin *et al.* reported that the silver heptamer structure exhibits a Fano resonance as a result of the interference between two modes, of which one is subradiant (or dark) and the other is superradiant (or bright).[8] The same behavior is expected in the gold heptamer except the frequencies would be shifted due to the difference in dielectric function between silver and gold. In the following presentation of our theoretical analysis, we use the nomenclature based on the group representation theory.[42] The heptamer structure discussed in this paper has the symmetry of point group D_{6h}. Consequently, the eigenmodes can be indexed by the irreducible representations of D_{6h}. Assuming the modes are excited by normally incident light with definite in-plane polarization, only the optically active in-plane modes are considered in this work. Among the irreducible representations of D_{6h}, E_{1u} is the only one with a net dipole moment and thus optically active. Furthermore, we consider only the two lowest energy E_{1u} modes in the unstressed gold heptamer

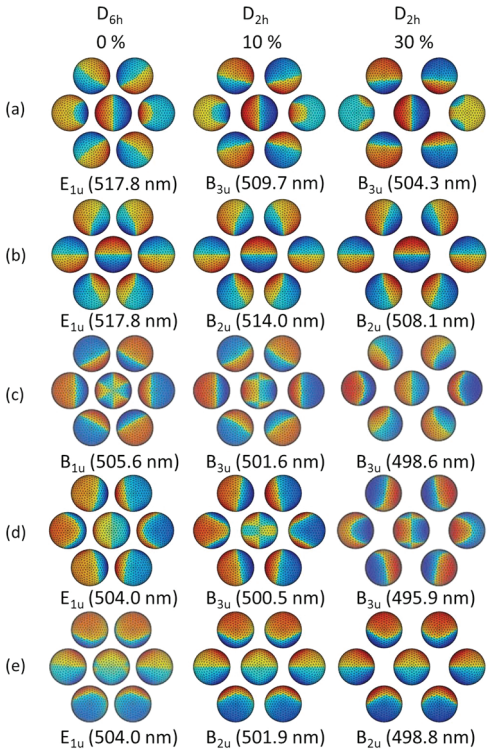

Figure 3. Evolution of charge distribution with uniaxial stress along the *x* direction. The first column shows the two lowest E_{1u} modes of the unstressed heptamer and the B_{1u} mode. The second and third columns show B_{2u} and B_{3u} modes of the heptamer under 10% and 30% strains, respectively. The resonance wavelengths of the heptamers are also shown.

structure because all higher modes are masked off by strong absorption by gold. In the first column of Figure 3, we show the charge distribution of the two lowest energy E_{1u} modes in an unstressed gold heptamer structure composed of seven identical gold spheres where the sphere diameter is 150 nm and gap between the spheres is 25 nm. Here the modes shown in Figure 3a,b belong to the lowest energy E_{1u} mode, and (d) and (e) to the second lowest E_{1u} mode. Note that the E_{1u} irreducible representation is a two-dimensional representation, and thus the E_{1u} modes are doubly degenerate with two orthogonal states having a net dipole moment in the *x* and *y* directions, respectively. Accordingly, the four charge distributions shown in the first column of Figure 3 possess a net dipole moment where (a) and (d) are *x*-dipoles and (b) and (e) are *y*-dipoles. Depending on the energy and the relative alignment of the dipole moment of the center sphere to those of the six satellite spheres, the E_{1u} modes can be classified as dark or bright modes. The lower energy E_{1u} mode shown in Figure 3a,b is a dark mode where the dipole moment of the center particle aligns against the dipole moments of satellite particles, making the total dipole moment small. On the other hand, the higher energy E_{1u} mode shown in Figure 3d,e is a bright mode where the dipole moments align

together to add up. The energies of these two E_{1u} modes were found to be 2.394 and 2.459 eV or 517.8 and 504.0 nm, respectively. These mode energy values would be accurate only for heptamers made of very small nanoparticles, as our model is valid in the static limit only. For larger sizes, retardation effects will shift and broaden the modes. The resultant overlap and interference between the two modes lead to a Fano resonance. The bright mode will broaden much more significantly than the dark mode, resulting in a Fano resonance that manifests itself in the form of a dip in the extinction spectrum, as observed in Figure 2.

When the heptamer is under uniaxial mechanical stress, the symmetry of the system is lowered to D_{2h}. The doubly degenerate E_{1u} mode splits into two nondegenerate modes belonging to B_{2u} and B_{3u} irreducible representations of the point group D_{2h}. Figure 3 shows the evolution of charge distribution as the mechanical stress is applied along the *x* direction. It clearly shows the original doubly degenerate modes split into *x*-dipole (B_{3u}) and *y*-dipole (B_{2u}) modes. Remarkably, the nature of the modes is mostly preserved. That is, the bright E_{1u} mode splits into bright B_{2u} and B_{3u} modes, while the dark E_{1u} mode spawns dark B_{2u} and B_{3u} modes. Also, all modes shift to shorter wavelengths with increasing mechanical strain values. However, the B_{3u} modes, which have dipole moment along the direction of mechanical stress, shift more than the B_{2u} modes, with dipole moment perpendicular to the mechanical stress. This leads to the polarization dependence, as the B_{3u} modes interact with *x*-polarized light and B_{2u} with *y*-polarized light. Therefore, as the heptamer is stretched along the *x* direction, *x*-polarized light would show resonance features in the shorter wavelengths than the *y*-polarized light. Even when the retardation effects are included and the resonance peaks broaden and shift, this general behavior survives and leads to the experimental observation in Figure 2: the dip in the extinction spectrum due to the Fano resonance blue-shifts for polarization parallel to the direction of mechanical stress but red-shifts for polarization perpendicular to it.

To confirm this, scattering and absorption cross sections were calculated for heptamers made of spherical gold particles with diameters ranging from 50 to 150 nm, using the generalized multiparticle Mie theory. For small sphere sizes, both the absorption and scattering spectra exhibit a single peak centered around 520 nm, which is a superposition of the two closely spaced E_{1u} modes. As the sphere sizes are increased, the two modes exhibit red shifts and broadening. The bright mode experiences strong radiation damping, and therefore it quickly disappears in the absorption spectra and produces a strong and broad band in the scattering spectra. The dark mode suffers from much less radiation damping and thus persists as a peak in the absorption spectra with relatively narrow line

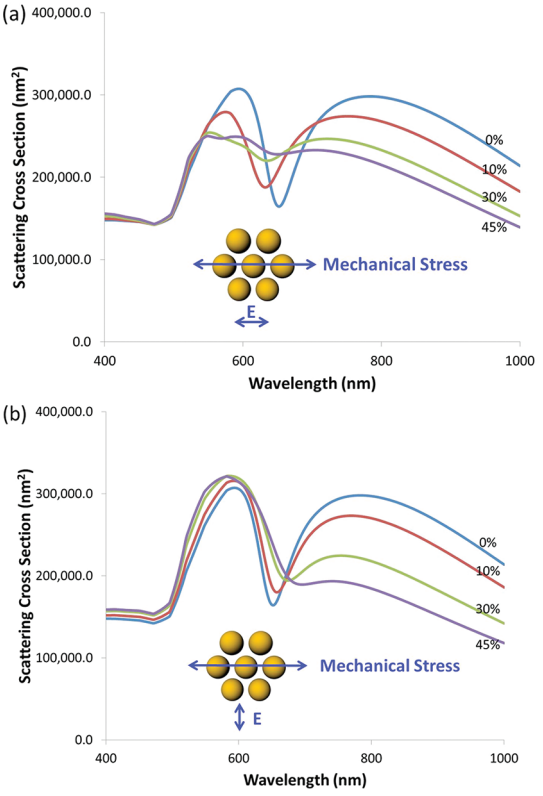

Figure 4. Scattering spectra of gold heptamers made of 150 nm spheres for (a) *x*-polarization and (b) *y*-polarization for various mechanical strain.

width. In the scattering spectra, the overlap between the two modes results in a dip, which is one of the well-known signatures of Fano resonances. For sphere diameters of 150 nm, both the absorption peak and the scattering dip occur at 650 nm.

When the heptamers are subject to uniaxial mechanical stress, the qualitative behaviors of the absorption and scattering spectra remain similar. However, the peak shift with increasing sphere diameters depends on the strain and polairzation. Figure 4 shows the scattering spectra for heptamers made of 150 nm gold spheres. With increasing mechanical stress along the *x* direction, the Fano resonance blue-shifts for *x* polarization but red-shifts for *y* polarization. The origin of this distinct polarization dependence can be traced back to the behaviors of B_{2u} and B_{3u} modes discussed earlier. The *y*-polarized light excites B_{2u} modes, which exhibit a much smaller blue shift than the B_{3u} modes, which are excited by the *x*-polarized light. The retardation effect in the large size heptamers then leads to red shifts, resulting in the B_{2u} mode shifting to the red of the original E_{1u} mode of the unstressed heptamer while the B_{3u} mode appears to the blue of the E_{1u} mode. Also, the dip remains distinct in the *y*-polarization spectra as the heptamer is stressed, whereas the dip becomes shallower with stretching in the *x*-polarization spectra. This behavior can also be seen from Figure 3a,b. The three modes shown in Figure 3b have almost

identical charge distributions, and this shows that the B_{2u} mode originating from the dark E_{1u} mode of the unstressed heptamer remains dark under mechanical stress. From this observation, we anticipate the Fano dip would remain distinct under mechnical stress for *y* polarization. In contrast, Figure 3a shows that the dark B_{3u} mode becomes brighter with stretching. Under mechanical stress along the *x* direction, the coupling between the three spheres along the *x* axis becomes significantly weaker. This leads to the dipole moments of the two spheres on either side of the center sphere almost vanishing and also the dipole moments of the upper and lower spheres aligning almost vertically. As a result, the *x*-dipole of the center sphere is no longer canceled by the surrounding spheres, and this consequently results in a diminishing dip in the scattering spectrum.

In addition to the diminishing Fano dip, the scattering spectra for *x* polarization also show an additional dip at shorter wavelengths. The additional dip is apparent in the spectra for 30% and 45% strain for *x* polarization but is clearly missing in all spectra for *y* polarization. This is a unique feature of heptamers under stress that has not been reported before. The origin of this second dip can be found by the group theoretical analysis. Briefly reiterating, in the unstressed heptamer structure possessing D_{6h} symmetry, only the E_{1u} modes have nonzero dipole moments and thus are optically active. When the symmetry is lowered to D_{2h} by uniaxial stress, the E_{1u} modes split into B_{2u} and B_{3u} modes, which interact with *x*- and *y*-polarized light, respectively. Since the unstressed heptamer has two E_{1u} modes in the frequency range of interest, we obtain two B_{2u} and two B_{3u} modes, producing a Fano resonance just as in the original unstressed heptamer. However, what is missing in this narrative is that the optically inactive B_{1u} mode in the unstressed heptamer becomes an optically active B_{3u} mode under uniaxial stress along the *x* direction. As shown in Figure 3c, the charge distribution calculated by the boundary integral method reveals that this B_{3u} mode is also a dark mode where the dipole moment of the center sphere aligns antiparallel against those of the satellite spheres, thereby producing a second Fano dip in the scattering spectra. In constrast, there are no other modes of the unstressed heptamer evolving into the B_{2u} mode within the frequency range we investigated, and thus we do not see any additional dip for the *y* polarization. In Figure 4a, the second dip in the *x*-polarized spectra is clearly observed only at large strain values. A possible reason the second dip is not resolved for small strain values is that the resonance wavelengths between the two B_{3u} modes arising from the B_{1u} and dark E_{1u} modes are too close to be resolved in the spectrum. The gold cylinder heptamer structure in Figure 2 showed the same general behavior, but in this system the second Fano resonance was present even for small strain values.

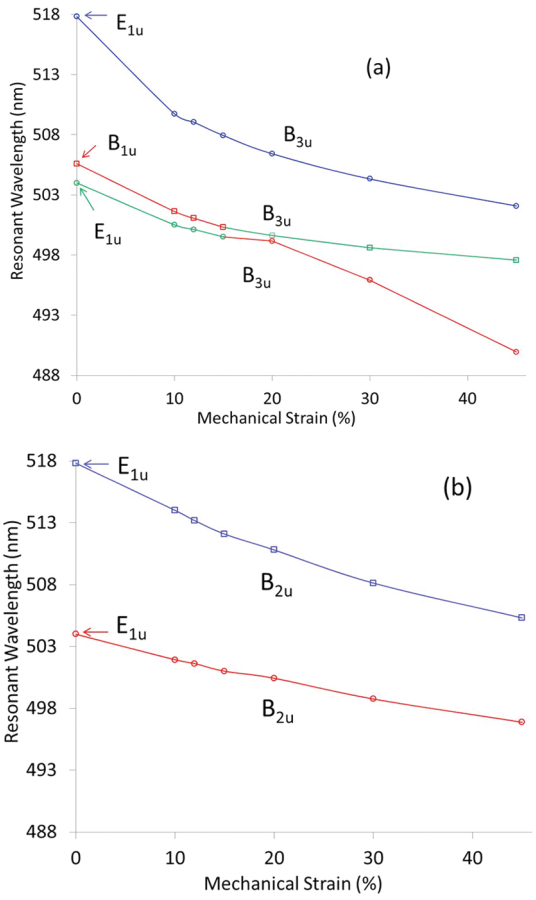

Figure 5. Resonant wavelengths of the three lowest energy optically active modes as a function of mechanical strain values. Only the modes interacting with *x* polarization are shown in (a), and the modes interacting with *y* polarization in (b). The resonance wavelengths are calculated for the heptamers made of 150 nm gold spheres by the boundary value integral method.

To gain further insight, we calculated the mode wavelengths of E_{1u} and B_{1u} modes of the unstressed heptamer by using the boundary integral method and followed how the wavelengths shift under mechanical stress. As shown in Figure 5, all modes exhibit blue shifts. For *y* polarization, the two E_{1u} modes simply shift to shorter wavelengths, as shown in Figure 5b. For *x* polarization, however, the behavior is complicated by the presence of a B_{1u} mode located close to the higher energy E_{1u} mode. As a result, while the low-energy E_{1u} mode remains largely isolated and shows a steady blue shift with increasing mechanical stress, the high-energy E_{1u} mode and B_{1u} mode, both of which become B_{3u} modes under stress, interact strongly and exhibit anticrossing behavior. As shown in Figure 5a, the B_{3u} mode arising from the B_{1u} mode stays at longer wavelengths than the B_{3u} mode spawned by the bright E_{1u} mode until the mechanical strain value exceeds 15%, but the order is reversed at higher strain values. Careful examination of charge distributions near the anticrossing point revealed that the charge distributions show clear signs of mixing between the two modes. As shown

in Figure 3c,d, when the heptamer is unstrained (0%), the B_{1u} and E_{1u} modes have distinct charge distributions. Among other things, the center particle of the E_{1u} mode arising from the B_{1u} mode has a hexapole-like charge distribution, while the center particle of the bright E_{1u} mode has a dipole-like charge distribution. For the mechanical strain values of 10% at which anticrossing occurs, the center particle of the two B_{3u} modes exhibits a hexapole-like charge distribution, clearly showing the mixing of the two modes. For a larger strain value of 30%, which occurs beyond anticrossing, the center particle of the lower B_{3u} mode in Figure 3c recovers the purely dipole-like charge distribution, whereas the higher B_{3u} mode in Figure 3d has a hexapole-like distribution. Charge distributions for additional strain values are provided in the Supporting Information, as further evidence of mode mixing. Additionally, the anticrossing behavior results in the middle B_{3u} mode wavelength becoming almost independent of applied stress at high strain values, while the highest energy B_{3u} mode continues to show significant blue shift with increasing mechanical stress. This result, combined with the retardation effect, explains why the longer wavelength Fano dip stops shifting to the blue but actually shows a slight red shift in Figure 4, whereas the shorter wavelength dip continues to show a blue shift.

Anticrossing of mutually interacting states is a universal phenomenon. In quantum physics, anticrossing of an interacting two-level system is well known.[43] Anticrossing is also routinely observed in optics. For example, anticrossing of a band-gap-guided mode and an index-guided mode in a photonic crystal waveguide is known to produce slow group velocity.[44] In plasmonics, anticrossing behavior due to the strong mixing between a molecular exciton and a surface plasmon polariton has been observed.[45] In our structure, anticrossing is observed as the interaction between the two B_{1u} modes is tuned by the applied mechanical stress. It is intriguing to discover that the originally optically inactive mode could become optically active under mechanical stress and strongly interact with the other optically active modes. This opens new possibilities for dynamically tuning and engineering resonances in the plasmonic nanostructures.

CONCLUSIONS

In conclusion, we have experimentally demonstrated dynamic tuning and symmetry lowering of the Fano resonance in a gold heptamer structure and presented an extensive theoretical study explaining the observed behaviors. The original unstressed heptamer structure exhibits a distinct dip in the optical extinction spectra due to the Fano resonance originating from the two interacting E_{1u} modes. When uniaxial stress is applied, the Fano dip blue-shifts for *x* polarization but red-shifts for *y* polarization. Furthermore, there appears a second dip for the *x* polarization when the mechanical stress is large. Group theoretical analysis showed that the uniaxial mechanical stress lowers the original D_{6h} symmetry of the heptamer to D_{2h}, and consequently the optically active doubly degenerate E_{1u} mode of the unstressed heptamer splits into B_{3u} and B_{2u} modes, which have *x*- and *y*-direction dipole moments and thus interact with *x*- and *y*-polarized light, respectively. Furthermore, the originally optically inactive B_{1u} mode of the unstressed heptamer becomes an optically active B_{3u} mode under mechanical stress and begins interacting strongly with a nearby B_{3u} mode, strongly influencing the optical spectra observed under mechanical stress. The charge distribution calculated by the boundary integral method in the static limit clearly showed how each mode shifts and interacts with other modes. Accounting for the retardation effects for larger sizes by using the multiparticle Mie theory, the experimentally observed behaviors were explained well and were also directly confirmed by the simulations using the finite element method.

Mechanical tuning of plasmonic nanostructures offers a new pathway to actively tunable nanophotonic devices. Mechanical tuning is particularly effective for plasmonic nanostructures exhibiting coupled plasmon resonance, which is highly sensitive to the structural parameters. Mechanical tuning also allows one to control the symmetry of a nanostructure, upon which optical properties are critically dependent. It is intriguing to discover that the originally optically inactive mode could become optically active under mechanical stress and strongly interact with the other optically active modes. This opens new possibilities for dynamically tuning and engineering resonances in plasmonic nanostructures. Dynamic tunability and on-demand control afforded by mechanically tunable nanophotonic devices could enable a new class of novel photonic devices.

METHODS

The heptamers were fabricated by an electron-beam lithography and lift-off process. The fabrication procedure started with a silicon wafer with a 100 nm Cr film thermally evaporated on it. The Cr layer serves as a protection layer for the PDMS membrane during the silicon dry etch process, preventing overetching and reducing undesirable cracks in the PDMS membrane. A bilayer of a polymethyl methacrylate (PMMA) resist and copolymer was coated on top of the Cr, and electron beam lithography was carried out to define the heptamer structure. Gold (80 nm) was then thermally evaporated onto the patterned resist, and the final gold heptamer structure was obtained by lift-off. A monolayer of (3-mercaptopropyl-)trimethoxysilane (MPTS) was deposited on the gold surface to function as an adhesion promotion layer and to improve contact between gold and PDMS.[18] Monolayer coating was carried out in a 1% solution of MPTS in methanol. After overnight immersion in the solution, the gold heptamer was rinsed

in methanol to remove excess MPTS on the surface. PDMS with a thickness of 850 μm was spin-coated on the heptamer structure to completely cover the heptamer structure and was cured at 100 °C for 2 h. Finally, the silicon substrate was completely dry etched by SF_6-based reactive ion etching, leaving the heptamer-embedded PDMS membrane with Cr protection layer at the bottom. After removal of 100 nm Cr, a completely free-standing PDMS membrane with a heptamer structure was obtained.

Mechanical stress was applied to the PDMS membrane by a custom-made device, where an aperture at the center is surrounded by a rigid frame and a linear translation stage controlled by a micrometer. The length, width, and height of the platform are 7.5, 5.0, and 1.3 cm, respectively. The aperture in the center over which the flexible heptamer structure is to be attached has a square shape with a side of 2.5 cm. One end of the PDMS membrane is glued to the rigid frame, and the other end to the movable translation stage with which mechanical stress is applied in a controlled fashion.

Conflict of Interest: The authors declare no competing financial interest.

Acknowledgment. This work was supported by National Science Foundation (BES 0608934).

Supporting Information Available: Additional information on the mechanical simulation, repeatability experiment, and charge distribution for additional strain value is available. This material is available free of charge *via* the Internet at http://pubs.acs.org.

REFERENCES AND NOTES

1. Pakizeh, T.; Kall, M. Unidirectional Ultracompact Optical Nanoantennas. *Nano Lett.* **2009**, *9*, 2343–2349.
2. Brown, L. V.; Sobhani, H.; Lassiter, J. B.; Norlander, P.; Halas, N. J. Heterodimers: Plasmonic Properties of Mismatched Nanoparticle Pairs. *ACS Nano* **2010**, *4*, 819–832.
3. Mastroianni, A. J.; Claridge, S. A.; Alivisatos, A. P. Pyramidal and Chiral Groupings of Gold Nanocrystals Assembled Using DNA Scaffolds. *J. Am. Chem. Soc.* **2009**, *131*, 8455–8459.
4. Zhang, Z.; Weber-Bargioni, A.; Wu, S. W.; Dhuey, S.; Cabrini, S.; Schuck, P. J. Manipulating Nanoscale Light Fields with Asymmetric Bowtie Nano-Colorsorter. *Nano Lett.* **2009**, *9*, 4505–4509.
5. Britt Lassiter, J.; Sobhani, H.; Fan, J. A.; Kundu, J.; Capasso, F.; Nordlander, P.; Halas, N. J. Fano Resonance in Plasmonic Nanoclusters: Geometrical and Chemical Tunability. *Nano Lett.* **2010**, *10*, 3184–3189.
6. Hentschel, M.; Saliba, M.; Vogelgesang, R.; Giessen, H.; Paul Alivisatos, A.; Liu, N. Transition from Isolated to Collective Modes in Plasmonic Oligomers. *Nano Lett.* **2010**, *10*, 2721–2726.
7. Fan, J. A.; Wu, C. H.; Bao, K.; Bao, J. M.; Bardhan, R.; Halas, N. J.; Manoharan, V. N.; Nordlander, P.; Shvets, G.; Cappasso, F. Self-Assembled Plasmonic Nanoparticle Clusters. *Science* **2010**, *328*, 1135–1138.
8. Mirin, N. A.; Bao, K; Nordlander, P. Fano Resonances in Plasmonic Nanoparticle Aggregates. *J. Phys. Chem. A* **2009**, *113*, 4028–4034.
9. Alonso-Gonzalez, P.; Schnell, M.; Sarriugarte, P.; Sobhani, H.; Wu, C.; Arju, N.; Khanikaev, A.; Golmar, F.; Albella, P.; Arzubiaga, L.; *et al*. Real-Space Mapping of Fano Interference in Plasmonic Metamolecules. *Nano Lett.* **2011**, *11*, 3922–3926.
10. Ou, F. S.; Hu, M.; Naumov, I.; Kim, A.; Wu, W.; Bratkovsky, A. M.; Li, X.; Williams, R. S.; Li, Z. Hot-Spot Engineering in Polygonal Nanofinger Assemblies for Surface Enhanced Raman Spectroscopy. *Nano Lett.* **2011**, *11*, 2538–2542.
11. Bao, K.; Mirin, N. A.; Nordlander, P. Fano Resonances in Planar Silver Nanosphere Clusters. *Appl. Phys. A: Mater. Sci. Process.* **2010**, *100*, 333–339.
12. Gallinet, B.; Martin, O. J. F. Influence of Electromagnetic Interactions on the Line Shape of Plasmonic Fano Resonances. *ACS Nano* **2011**, *5*, 8999–9008.
13. Dregely, D.; Hentschel, M.; Giessen, H. Excitation and Tuning of Higher-Order Fano Resonances in Plasmonic Oligomer Clusters. *ACS Nano* **2011**, *5*, 8202–8211.
14. Yan, B.; Boriskina, S. V.; Reinhard, B. M. Optimizing Gold Nanoparticle Cluster Configurations ($n \leq 7$) for Array Applications. *J. Phys. Chem. C* **2011**, *115*, 4578–4583.
15. Park, W.; Lee, J.-B. Mechanically Tunable Photonic Crystal Structure. *Appl. Phys. Lett.* **2004**, *85*, 4845–4847.
16. Wong, C. W.; Rakich, P. T.; Johnson, S. G.; Qi, M.; Smith, H. I.; Ippen, E. P.; Kimerling, L. C.; Jeon, Y.; Barbastathis, G.; Kim, S.-G. Strain-Tunable Photonic Band Gap Microcavities in Optical Waveguides. *Appl. Phys. Lett.* **2004**, *84*, 1242–1244.
17. Cui, Y.; Tamma, V. A.; Lee, J.-B.; Park, W. Mechanically Tunable Negative-Index Photonic Crystal Lens. *IEEE Photonics J.* **2010**, *2*, 1003–1012.
18. Pryce, I. M.; Aydin, K.; Kelaita, Y. A.; Briggs, R. M.; Atwater, H. A. Highly Strained Compliant Optical Metamaterials with Large Frequency Tunability. *Nano Lett.* **2010**, *10*, 4222–4227.
19. Ou, J. Y.; Plum, E.; Jiang, L.; Zheludev, N. I. Reconfigurable Photonic Metamaterials. *Nano Lett.* **2011**, *11*, 2142–2144.
20. Huang, F.; Baumberg, J. J. Actively Tuned Plasmons on Elastomerically Driven Au Nanoparticle Dimers. *Nano Lett.* **2010**, *10*, 1787–1792.
21. Fano, U. Effects of Configuration Interaction on Intensities and Phase Shifts. *Phys. Rev.* **1961**, *124*, 1866–1878.
22. Bulka, B. R.; Stefanski, P. Fano and Kondo Resonance in Electronic Current through Nanodevices. *Phys. Rev. Lett.* **2001**, *86*, 5128–5131.
23. Kobayashi, K.; Aikawa, H.; Sano, A.; Katsumoto, S.; Iye, Y. Fano Resonance in a Quantum Wire with a Side-Coupled Quantum Dot. *Phys. Rev. B* **2004**, *70*, 035319.
24. Ladron de Guevara, M. L.; Claro, F.; Orellana, P. A. Ghost Fano Resonance in a Double Quantum Dot Molecule Attached to Leads. *Phys. Rev. B* **2003**, *67*, 195335.
25. Hao, F.; Sonnefraud, Y.; Van Dorpe, P.; Maier, S. A.; Halas, N. J.; Nordlander, P. Symmetry Breaking in Plasmonic Nanocavities: Subradiant LSPR Sensing and a Tunable Fano Resonance. *Nano Lett.* **2008**, *8*, 3983–3988.
26. Hao, F.; Nordlander, P.; Sonnefraud, Y.; Van Dorpe, P.; Mailer, S. A. Tunability of Subradiant Dipolar and Fano-Type Plasmon Resonance in Metallic Ring/Disk Cavities: Implications for Nanoscale Optical Sensing. *ACS Nano* **2009**, *3*, 643–652.
27. Verellen, N.; Sonnefraud, Y.; Sobhani, H.; Hao, F.; Moshchalkov, V. V.; Van Dorpe, P.; Nordlander, P.; Maier, S. A. Fano Resonances in Individual Coherent Plasmonic Nanocavities. *Nano Lett.* **2009**, *9*, 1663–1667.
28. Liu, N.; Langguth, L.; Weiss, T.; Kastel, J.; Fleischhauer, M.; Pfau, T.; Giessen, H. Plasmonic Analogue of Electromagnetically Induced Transparency at the Drude Damping Limit. *Nat. Mater.* **2009**, *8*, 758–762.
29. Christ, A.; Ekinci, Y.; Solak, H. H.; Gippius, N. A.; Tikhodeev, S. G.; Martin, O. J. F. Controlling the Fano Interference in a Plasmonic Lattice. *Phys. Rev. B* **2007**, *76*, 201405(R).
30. Lukyanchuk, B.; Zheludev, N. I.; Maier, S. A.; Halas, N. J.; Norlander, P.; Giessen, H.; Chong, C. T. The Fano Resonance in a Plasmonic Nanostructures and Metamaterials. *Nat. Mater.* **2010**, *9*, 707–715.
31. Bachelier, G.; Russier-Antoine, I.; Benichou, E.; Jonin, C.; Del Fatti, N.; Vallee, F.; Brevet, P.-F. Fano Profiles Induced by Near-Field Coupling in Heterogeneous Dimers of Gold and Silver Nanoparticles. *Phys. Rev. Lett.* **2008**, *101*, 197401.
32. Tetz, K. A.; Pang, L.; Fainman, Y. High-Resolution Surface Plasmon Resonance Sensor Based on Linewidth-Optimized Nanohole Array Transmittance. *Opt. Expr.* **2006**, *31*, 1528–1530.
33. Chuntonov, L.; Haran, G. Trimeric Plasmonic Molecules: The Role of Symmetry. *Nano Lett.* **2011**, *11*, 2440–2445.
34. Chuntonov, L.; Haran, G. Effect of Symmetry Breaking on the Mode Structure of Trimeric Plasmonic Molecules. *J. Phys. Chem. C* **2011**, *115*, 19488–19495.
35. Johnson, P. B.; Christy, R. W. Optical Constants of the Noble Metals. *Phys. Rev. B* **1972**, *15*, 4370.
36. Volker, C. A.; Lilleodden, E. T. Size Effects in the Deformation of Sub-Micron Au Columns. *Philos. Mag.* **2006**, *86*, 5567–5579.

37. Robinson, R. G. R.; Stephens, K. G.; Wilson, I. H. The Effect of Ion Bombardment on the Strain Gauge Factor of Thin Gold Films. *Thin Solid Films* **1975**, *27*, 251–262.
38. Armani, D.; Liu, C.; Aluru, N. Re-Configurable Fluid Circuits by PDMS Elastomer Micromachining. *Proc. IEEE MEMS99* **1999**, 222–227.
39. Mayergoyz, I. D.; Fredkin, D. R.; Zhang, Z. Electrostatic (Plasmon) Resonances in Nanoparticles. *Phys. Rev. B* **2005**, *72*, 155412.
40. Gomez, D. E.; Venron, K. C.; Davis, T. J. Symmetry Effects on the Optical Coupling between Plasmonic Nanoparticles with Applications to Hierarchical Structures. *Phys. Rev. B* **2010**, *81*, 075414.
41. Yu, Y. I.; Gustafson, B. A. S. A Generalized Multiparticle Mie-Solution: Further Experimental Verification. *J. Quantum Spectrosc. RA.* **2001**, *70*, 395.
42. Tinkham *Group Theory and Quantum Mechanics*; McGraw-Hill, 1964.
43. Feynman, R. P.; Leighton, R. B.; Sands, M. In *The Feynman Lectures, Vol. 3. Quantum Mechanics*; Addison-Wesley Publishing Co.: London, 1970; Chapters 9−11.
44. Notomi, M.; Yamada, K.; Shinya, A.; Takahashi, J.; Takahashi, C.; Yokohama, I. Extremely Large Group-Velocity Dispersion of Line-Defect Waveguides in Photonic Crystal Slabs. *Phys. Rev. Lett.* **2001**, *87*, 253902.
45. Dintinger, J.; Klein, S.; Bustos, F.; Barnes, W. L.; Ebbesen, T. W. Strong Coupling between Surface Plasmon-Polaritons and Organic Molecules in Subwavelength Hole Arrays. *Phys. Rev. B* **2005**, *71*, 035424.